

To be published in *Astrophys. Journal*

High Redshift Quasars and Star Formation in the Early Universe *

M. Dietrich ^{1,2} I. Appenzeller ² M. Vestergaard ³ S.J. Wagner ²

dietrich@astro.ufl.edu

ABSTRACT

In order to derive information on the star formation history in the early universe we observed 6 high-redshift ($z \simeq 3.4$) quasars in the near-infrared to measure the relative iron and Mg II emission strengths. A detailed comparison of the resulting spectra with those of low-redshift quasars show essentially the same Fe II/Mg II emission ratios and very similar continuum and line spectral properties, indicating a lack of evolution of the relative iron to magnesium abundance of the gas since $z \simeq 3.4$ in bright quasars. On the basis of current chemical evolution scenarios of galaxies, where magnesium is produced in massive stars ending in type II SNe, while iron is formed predominantly in SNe of type Ia with a delay of ~ 1 Gyr and assuming as cosmological parameters $H_0 = 72 \text{ km s}^{-1} \text{ Mpc}^{-1}$, $\Omega_M = 0.3$, and $\Omega_\Lambda = 0.7$, we conclude that major star formation activity in the host galaxies of our $z \simeq 3.4$ quasars must have started already at an epoch corresponding to $z_f \simeq 10$, when the age of the universe was less than 0.5 Gyrs.

Subject headings: galaxies: quasars — galaxies: high-redshift — galaxies: Fe II emission — galaxies: elemental abundance

¹Department of Astronomy, University of Florida, 211 Bryant Space Center, Gainesville, FL 32611-2055, USA

²Landessternwarte Heidelberg–Königstuhl, Königstuhl 12, D–69117 Heidelberg, Germany

³Department of Astronomy, The Ohio State University, 140 West 18th Av., Columbus, OH 43210-1173, USA

* Based on observations collected at the European Southern Observatory, La Silla, Chile

1. Introduction

Quasars are among the most luminous objects in the universe. Because of their high luminosity, bright quasars can be observed at practically any distance at which these objects are expected to occur. Among the characteristic properties of quasars are prominent emission lines from the gas ionized and heated by a central radiation source. Assuming that this gas originates from the interstellar medium of the quasar host galaxies, line diagnostics applied to the prominent emission lines provide an important tool to study the chemical composition and enrichment history of the quasar host galaxies at all cosmological epochs. Earlier studies of the emission line spectra have demonstrated that quasars at redshift $z \geq 3$ have metallicities of up to an order of magnitude larger than the solar value (e.g., Hamann & Ferland 1992, 1993, 1999; Ferland et al. 1996; Korista et al. 1996; Pettini 1999; Dietrich et al. 1999; Dietrich & Wilhelm-Erkens 2000). These results show that well before the epoch corresponding to $z = 3$ significant star formation must have taken place in the galactic or proto-galactic cores where these quasars reside.

Some information on the exact epoch of the first star formation activity in these objects can be derived from the relative abundance of α -process elements and iron. According to present chemical enrichment scenarios α -element nuclei are produced predominantly in type II SNe with massive progenitors on time scales of $\tau_{evol} \simeq 2 \cdot 10^6 - 10^7$ years after the beginning of the star formation epoch. On the other hand, the dominant source of iron is assumed to be type Ia SNe at the end point of the evolution of intermediate mass stars in binary systems, about $\tau_{evol} \simeq 1$ Gyr after the onset of the star formation epoch (e.g., Tinsley 1979; Matteucci & Greggio 1986; Wheeler et al. 1989; Yoshii et al. 1996). The amount of iron returned to the interstellar medium in SN II ejecta is rather low (Yoshii et al. 1996, 1998). The significantly different time scales of the release of α -elements and iron to the interstellar medium results in a time delay of the order of ~ 1 Gyr in the Fe II enrichment. Detecting Fe II emission at high redshift comparable to the relative strength observed in quasars at lower redshift indicates that the formation of the stars which had released the iron had occurred at least ~ 1 Gyr earlier. Therefore, the line ratio of α -element vs. iron emission can be used as a cosmological clock.

Given the complexity of the Fe II emission spectrum accurate iron abundances are not yet easy to deduce and the full synthesis of the individual AGN spectra is required (Verner et al. 1999) which seriously complicates such measurements. However, the UV Fe II multiplets around Mg II ($\lambda\lambda \sim 2000 - 3000 \text{ \AA}$), the most common strong iron multiplets among AGNs (Wills et al. 1980; Grandi 1981; Netzer et al. 1985), are probably the most promising for obtaining at least some information on the relative iron abundance (e.g., Wampler & Oke 1967; Wills et al. 1985; Hamann & Ferland 1999). A suitable spectral feature for

testing the presence of α -elements is the Mg II resonance doublet at $\lambda\lambda 2795, 2803 \text{ \AA}$ (hereafter Mg II $\lambda 2798$). Since Mg II and Fe II have similar ionization potentials and are expected to originate in the same partially ionized zone of the excited gas, the ratio of these lines provides a valuable measure to estimate the α -element vs. iron abundance ratio, at least on a relative scale (Hamann & Ferland 1999). Observations of the Mg II $\lambda 2798$ and of the rest-frame UV-multiplets of Fe II in the spectra of several high-redshift quasars have been published by Hill et al. (1993), Elston et al. (1994), Kawara et al. (1996), Taniguchi et al. (1997), Yoshii et al. (1998), Murayama et al. (1998), Murayama et al. (1999), Thompson et al. (1999), Kuhn et al. (2001), and Green et al. (2001). Generally, fairly strong Fe II emission was found, indicating a very early cosmic epoch of the first star formation in the high- z quasar host galaxies.

In order to derive more accurate and more quantitative information on the first star formation epoch in such objects we studied a small sample of six quasars with redshifts $z \simeq 3.4$ using uniformly processed and analyzed high-quality near infrared spectra covering (in the observer’s frame) the wavelength range ($1.0 \lesssim \lambda \lesssim 2.5 \mu\text{m}$). The quasars were selected to be accessible at the time of observation and to be bright enough to be observed within reasonable integration times with ESO’s 3.5 m NTT. Assuming $H_0 = 72 \text{ km s}^{-1} \text{ Mpc}^{-1}$, $\Omega_M = 0.3$, $\Omega_\Lambda = 0.7$ (Carroll et al. 1992; Carlberg et al. 1999; Perlmutter et al. 1999; Freedman et al. 2001) this redshift corresponds to a cosmic epoch of $\sim 1.8 \text{ Gyrs}$, i.e. about 10% of the current cosmic age. For the selected redshifts the strong Mg II $\lambda 2798$ emission line and most of the strong ultraviolet Fe II emission at $\lambda\lambda 2300 - 2600 \text{ \AA}$ are redshifted into the NIR J-band, while the $H\beta$ and $[\text{O III}]\lambda\lambda 4959, 5007$ lines together with the optical Fe II emission are shifted to the K-band wavelength region.

We covered practically the whole restframe wavelength range $\lambda\lambda 2100 - 5600 \text{ \AA}$ continuously. This made it possible to derive reliable continuum fits and, thus, at least internally rather accurate flux values for the ultraviolet and optical Fe II emission.

2. Observations and Data Analysis

The coordinates, redshifts, and the apparent brightness of the six quasars are listed in Table 1. All observations were carried out on Oct. 19 – 22, 1999 using the SofI (Son of ISAAC) NIR spectrometer and camera attached to the 3.5 m NTT telescope of the European Southern Observatory at La Silla, Chile. The seeing was typically $\approx 1''$ during the first three nights and $\approx 1''.7$ during the fourth night. The detector was a 1024×1024 Hawaii HgCdTe array. All spectra were recorded in the longslit mode ($1'' \times 290''$). The pixel scale was $0''.267/\text{pixel}$. To obtain the entire near infrared spectral range from $\sim 0.95 \mu\text{m}$ to $\sim 2.5 \mu\text{m}$

we used the blue grism ($0.95 - 1.64\mu\text{m}$) and the red grism ($1.52 - 2.52\mu\text{m}$) in first order. This setting provides a reasonable spectral overlap in the H-band region ($\approx 0.12\mu\text{m}$). For flux calibration and correction of the strong atmospheric absorption features we observed the standard stars listed in Table 1 (Elias et al. 1982; Perryman et al. 1998) several times during each night.

The observing epochs and exposure times for the quasars and standard stars are listed in Table 2. Making use of the SofI long-slit mode we changed the location of the object along the slit by $60''$ (with an additional random offset within $5''$) for subsequent exposures to optimize the sky-correction.

The dark frames were recorded with the same exposures time as the science frames. The average dark frames of a specific exposure time were spatially extracted and the 1D countrate distributions were fitted with a low-order polynomial. The low-order polynomial fits were subtracted to correct for the dark current signal.

For wavelength calibration we took xenon-neon comparison spectra in the blue and red setting of the gratings in lamp on and lamp off mode. The latter measures the IR background contamination. Its subtraction allows access to weaker spectral lines. Because the location of the spectral lines were reproduced within less than 0.3 pixels, we used a single XeNe-spectrum for the wavelength calibration for all three nights. In the blue wavelength range ($0.95 - 1.64\mu\text{m}$) the 2D wavelength calibration based on 19 spectral lines yielded a pixel scale of 6.93 \AA/pixel and a wavelength mean error of 0.50 \AA . For the red wavelength range ($1.52 - 2.52\mu\text{m}$) the corresponding values (based on 16 spectral lines) are 10.19 \AA/pixel and 0.83 \AA . The FWHM spectral resolution measured using strong night sky emission lines was about $R \simeq 600$ (blue) and $R \simeq 700$ (red).

Flatfield frames taken with the internal lamps turned out not to be usable because of offsets (of up to 4 columns in the spatial direction). Furthermore, normalized dome flatfield exposures of the same night introduced additional structures on large scales. Therefore, we used the science exposures to compute a sky flatfield for the flatfield correction. Since, due to our observing strategy, the location of an object was different for each individual exposure, we computed the median of the normalized science frames. These median frames were used to compute a normalized sky flatfield according to the procedure outlined by Horne (1986). These flatfield frames were used to apply the 2D flatfield correction to the science frames.

We derived and subtracted the night sky intensity for each frame individually because the night sky intensity showed significant variations on time scales of 180 sec - 240 sec. For this purpose a 3^{rd} order polynomial fit was calculated for each wavelength element to fit the spatial intensity distribution of the night sky emission. The fit was based on $22''$ wide

regions which were at least $5''$ separated from the targets, quasar and standard star, both of which were point source like. The remaining residua after the sky correction were removed by subtracting the object-free part of a sky-corrected frame containing the same residua.

The observed standard stars were used to correct the strong atmospheric absorption bands separating the J- and H-band and the H- and K-band, respectively, and other atmospheric (absorption) features. The range of the atmospheric transmission properties during the observing run is shown in Fig. 1.

To obtain a sensitivity function to transform the observed count rates to flux units we assumed that the IR spectral energy distribution of a A-type star and G-type star can be described with a black body energy distribution of a specific T_{eff} . We used the black body temperatures given by Kurucz (1992) for the different spectral types of the stars we observed. We applied $T_{eff}=5850$ K (HD 25402, HD 210395), $T_{eff}=8250$ K (HD 19904, HD 205772), and $T_{eff}=9750$ K (HD 38921) to compute a black body energy distribution for the observed wavelength range. Next, these black body spectra were scaled to match the apparent magnitudes of the observed standard stars in the J-, H-, and K-band. For each standard star a sensitivity curve was calculated. For HD 25402 and HD 210395 we had to calculate the apparent near infrared magnitudes based on the apparent V-band magnitude while for HD 19904, HD 38921, and HD 205772 we could use the J,H, and K magnitudes given by Elias et al. (1982). In general, the sensitivity functions given for these two subsets are identical within less than 4% . But they differ by $\sim 10\%$ at the long wavelength end of the blue and red wavelength range. Hence, we used the J,H,K-band based sensitivity functions provided by HD 19904, HD 38921, and HD 205772 to derive a mean sensitivity function for the blue and red wavelength ranges.

The quasar spectra were extracted using the Horne (1986) extraction routine. The width of the spatial profile for the quasar spectra was the same as measured for the stars. Hence, the quasar spectra were treated as point sources. Since some individual spectra of low quality were eliminated during the coaddition procedure, the effective integration time for the quasars is somewhat lower than the sum of the individual exposure times (Tables 2,3).

The individual spectra of the quasars were corrected for atmospheric absorption using appropriately scaled transmission functions provided by observed spectra of the standard stars.

To correct for cosmic-ray events the individual 1D spectra were compared with one another. We calculated for each wavelength element the mean and standard deviation among the available 1-D spectra, excluding the smallest and largest flux measurement. If these

excluded measurements deviate by more than three times the standard deviation, they were replaced by the calculated mean value, respectively. For each quasar weighted mean spectra were calculated. The weight was given by the mean signal-to-noise ratio in the continuum across the spectrum. Finally, we transformed the quasar spectra to those emitted in the quasar restframe. Following Peterson (1997) the flux conversion was carried out according to

$$F'_{obs}(\lambda_o) = F_{rest}(\lambda_1)/(1+z)^3$$

The resulting restframe quasar spectra are displayed in Fig. 2.

3. Modelling of the Quasar Spectra

While at least the narrow emission component of the strong and relatively isolated Mg II $\lambda 2798$ doublet appears to be measured easily in QSO spectra, the Fe II emission forms broad emission blends caused by the superposition of several ten thousand discrete lines and the intrinsically large quasar emission line widths (e.g., Wills et al. 1985, hereafter WNW85; Verner et al. 1999). Due to the large number of merging lines and the difficulty of deriving a local continuum level, it is not possible to measure these lines individually. However, as suggested and demonstrated by WNW85, it is possible to derive the Fe II emission strength by decomposing the quasar spectrum into several well defined components. Therefore, we assumed our observed spectra to consist of a superposition of the following four components, (i) a power law continuum ($F_\nu \sim \nu^\alpha$), (ii) Balmer continuum emission, (iii) a pseudo-continuum due to merging Fe II emission blends, and (iv) an emission spectrum of other individual broad emission lines.

3.1. Non-stellar Continuum

We first determined component (i), the underlying non-stellar power law continuum, from spectral windows which are free (or almost free) of contributions by the components ii to iv. For this purpose it was very important to have spectra covering the (rest frame) optical region up to $\sim 5500 \text{ \AA}$ with one of the continuum windows at $\sim 5100 \text{ \AA}$, which is nearly free of emission line contamination and hydrogen continua. Only minor Fe II-emission can be expected for this wavelength region (WNW85; Verner et al. 1999) and so will not significantly affect the continuum setting. For three of our quasars (Q 0103-260, Q 0256-0000, and Q 0302-0019) we also have restframe UV spectra available, covering O VI $\lambda 1034$ to

C III] $\lambda 1909$ (Dietrich & Hamann 2001) with continuum windows at $\lambda \approx 1330 - 1380 \text{ \AA}$ and $\lambda \approx 1440 - 1470 \text{ \AA}$ which are nearly uncontaminated by line emission as well (Verner et al. 1999). For those quasars where we had no access to the short wavelength UV part of the spectrum we used continuum windows at $\sim 2100 \text{ \AA}$ to estimate the continuum strength. The uncertainty introduced by estimating the continuum based on at least two of the spectral ranges described above, is estimated to be of the order of $\sim 10\%$.

The UV data allow us even better constraints to be placed on the non-stellar continuum for these objects.

3.2. Balmer Continuum

The Balmer continuum emission was modeled according to the following procedure: Assuming case B conditions the flux ratio of the integrated Balmer continuum emission (BaC) and of $H\beta \lambda 4861$ is given by $I(\text{BaC})/I(H\beta) = 3.95 T_4^{0.4}$, with T in units of 10^4 K (e.g., WNW85). But for significant optical depth in the Balmer emission lines and especially in the Balmer continuum, large deviations from this simple relation are expected. Optically thick Balmer continuum emission can be described by a blackbody spectrum at all wavelengths (e.g., Malkan & Sargent 1982). But since the absorption cross section decreases as $(\nu/\nu_{BE})^3$, the continuum emission will become optically thin at some wavelength. To get an estimate of the Balmer continuum emission spectrum for the purpose of model fitting we assumed clouds of uniform temperature ($T_e = 15000 \text{ K}$) which are partially optically thick. In this case the Balmer continuum spectrum can be described by

$$F_\nu^{\text{BaC}} = F_\nu^{\text{BE}} B_\nu(T_e)(1 - e^{-\tau_\nu}); \quad \nu \geq \nu_{BE}$$

with $B_\nu(T_e)$ as the Planck function at the electron temperature T_e (Grandi 1982). τ_ν is the optical depth at the frequency ν . τ_ν can be calculated in terms of the optical depth τ_{BE} at the Balmer edge using

$$\tau_\nu = \tau_{BE} \left(\frac{\nu}{\nu_{BE}} \right)^{-3}$$

and F_ν^{BE} is a normalized estimate for the Balmer continuum flux density at the Balmer edge at $\lambda = 3646 \text{ \AA}$.

After subtraction of the power-law continuum component, the strength of the Balmer continuum emission can be estimated from the flux density at $\lambda \simeq 3675 \text{ \AA}$, since at this wavelength there is no significant contamination by Fe II emission (WNW85; Verner et al. 1999). The

$\lambda 3675 \text{ \AA}$ restframe flux density level was therefore used to normalize the Balmer continuum spectrum. At wavelengths $\lambda \geq 3646 \text{ \AA}$ higher order Balmer lines are merging to a pseudo-continuum, yielding a smooth rise to the Balmer edge (WNW85). We used the results of the model calculations provided by Storey & Hummer (1995) (case B, $T_e = 15000 \text{ K}$, $n_e = 10^8 - 10^{10} \text{ cm}^{-3}$). We calculated several Balmer continuum spectra for $T_e = 15000 \text{ K}$ and $0.1 \leq \tau_\nu \leq 2$ to obtain Balmer continuum template spectra. These Balmer continuum templates were supplemented for $\lambda > 3646 \text{ \AA}$ with high order Balmer emission lines with $10 \leq n \leq 50$, i.e. $H\vartheta$ and higher.

3.3. Fe II Emission

Calculating the Fe II emission spectrum, is much more difficult and the influence of unknown parameters such as metalicity, pumping by the incident continua, line fluorescence, emission line transport and turbulence velocities, which affect the emergent Fe II spectrum, are still not well understood (e.g., WNW85; Netzer et al. 1985; Bautista & Pradhan 1998; Sigut & Pradhan 1998; Verner et al. 1999; Collin & Joly 2000). However, in spite of these uncertainties WNW85, Laor et al. (1997), and McIntosh et al. (1999) and others have shown that the Fe II emission spectrum of Seyfert 1 galaxies and quasars can be modelled. Therefore, we fitted the Fe II emission in our quasar spectra using scaled and broadened empirical Fe II emission template spectra to derive relative Fe II emission strength values. For the ultraviolet wavelength range these templates had been extracted from HST observations of I Zw 1 by Vestergaard & Wilkes (2001). The optical Fe II-emission template, extracted from ground-based spectra of I Zw 1, was kindly provided by T. Boroson.

3.4. Strong Broad Emission Lines

The broad emission lines of $\text{Mg II } \lambda 2798$ and of $\text{H}\beta \lambda 4861$ were fitted in our spectra with Gaussian components to measure the integrated line flux. Generally, the $\text{Mg II } \lambda 2798$ emission line profile could be reconstructed with two Gaussian components, one narrow and one broad and blueshifted. For the $\text{H}\beta \lambda 4861$ emission line profile we used the same approach. While the width of the narrow components in both lines tend to be of the same order ($\text{FWHM}(\text{Mg II}) = 2850 \pm 460 \text{ km s}^{-1}$ and $\text{FWHM}(\text{H}\beta) = 2950 \pm 360 \text{ km s}^{-1}$), the broad component which we used for $\text{H}\beta$ was significantly broader than for Mg II ($\text{FWHM}(\text{H}\beta) = 10000 \pm 1000 \text{ km s}^{-1}$ and $\text{FWHM}(\text{Mg II}) = 6200 \pm 700 \text{ km s}^{-1}$). However, the approach to reconstruct the Mg II and $\text{H}\beta$ emission line profiles with two Gaussian components was only chosen to measure the line flux; each individual component has no physical meaning by itself.

3.5. Internal Reddening

The effect of internal reddening on broad-emission lines is still unclear. In recent years growing evidence has appeared for the presence of large amounts of dust ($M_{dust} \gtrsim 10^8 M_{\odot}$) in the host galaxies of high redshift quasars (e.g., Guilleaume et al. 1997, 1999; Carilli et al. 2000; Omont et al. 2001). It is assumed that the dust is distributed in a kiloparsec-scale warped disk (Sanders et al. 1989) which is illuminated by the central AGN. The observed dust emission spectra from 3 to 30 μm can be explained by such a model as shown by Andreani et al. (1999) and Willott et al. (2000). However, since the present spectra are typical quasar spectra with prominent broad emission lines, it is unlikely that the Broad-Line Region is significantly blocked by dust (e.g., Netzer & Laor 1993). Even if the radiation has to pass through an (external) dust screen the extinction of the Mg II and the UV Fe II-emission (having about the same mean wavelength) will be comparable and the line ratio is not expected to be significantly modified. However, in the case of dust located within the line emitting gas, the situation is more complicated. Since Mg II $\lambda 2798$ has a larger optical depth than that of the Fe II-emission, the Mg II line emission will suffer more resonance scattering, resulting in a longer effective internal lightpath, and thus be more weakened than the Fe II-emission. This would result in a larger Fe II/Mg II ratio. To investigate the influence of internal dust reddening, detailed model calculations are required. Such calculations are beyond the scope of the current paper; however this effect will be investigated for an upcoming study of the evolution of the Fe II/Mg II ratio for quasars at redshifts of $0 < z < 5$.

4. Results

The results of our analysis are given in Figs. 3 – 5 and in Table 4. We fitted five spectral wavelength ranges ($\lambda \sim 2200 - 2750 \text{ \AA}$, $\sim 2860 - 3080 \text{ \AA}$, $\sim 3400 - 3650 \text{ \AA}$, $\sim 4500 - 4650 \text{ \AA}$, $\sim 5050 - 5400 \text{ \AA}$) in the quasar spectra. These windows were selected since they correspond to the spectral range of our template spectra and are not too strongly affected by atmospheric absorption in our IR-spectra. The strength of the Fe-emission templates was varied. We also varied the strength and the optical depth τ_{ν} of the Balmer continuum emission as indicated above. We calculated a minimal χ^2 to determine the best fit. In order to estimate the accuracy of our fits, we calculated fits also for a sample of different parameters around the best fit values and we determined χ^2 as a function of the parameter values. From the widths of the resulting χ^2 distributions we then calculated mean errors for these parameters.

To compare the spectral properties of the high- z quasars with the quasar population at lower redshift, we calculated a local mean quasar spectrum. This quasar spectrum consists of 101 quasars which were taken from a large quasar sample (Dietrich & Hamann 2001).

The quasars were selected to have $z \leq 2$ and to cover a luminosity range comparable to the $z \simeq 3.4$ quasars under study. The criterion of comparable luminosity minimizes luminosity effects on the emission line strength like the Baldwin effect (e.g., Osmer & Shields 1999). The average luminosity of the quasars which contribute to the local mean quasar spectrum amounts to $\log \lambda L_{\lambda}(1450\text{\AA}) = 43.5 \pm 0.3 \text{ erg s}^{-1}$. The average luminosity of the six high- z quasars is $\log \lambda L_{\lambda}(1450\text{\AA}) = 43.9 \pm 0.2 \text{ erg s}^{-1}$.

In Fig. 3 and 4 we present the multicomponent fit for the six high- z quasar spectra and in Fig. 5 for the local mean quasar spectrum. The individual components are also shown together with the fit. In addition, the resulting residuum spectra are displayed, too. Although the observed quasar spectra are well represented by the multicomponent models, several broad emission features can be seen in the residua. The broad residuum in the wavelength range $\lambda \simeq 3800 - 4000 \text{ \AA}$ is caused by the Balmer emission lines H δ up to H η , because the BaC emission template we used includes Balmer emission lines with $10 \leq n \leq 50$. The second strong residual emission at $\lambda \simeq 3200\text{\AA}$ is associated with the Fe II-emission blends M6, M7 which are not included in the ultraviolet Fe-emission template we used. In the residuum spectra of Q 0103-260, Q 0302-0019, and of the local mean quasar spectrum some emission is detected for $\lambda \lesssim 2200\text{\AA}$. This additional emission can be ascribed to Fe II-emission which is not contained in our Fe-emission template but can be expected on the basis of model calculations (Verner et al. 1999).

In addition to the relative flux of the Fe-emission blends we list in Table 4 also flux values for some other permitted and forbidden emission lines of interest in the observed wavelength interval. The flux is given in units of the corresponding Mg II $\lambda 2798$ flux (i.e. the table lists in all cases the ratio between the observed emission flux and the flux of the Mg II $\lambda 2798$ line observed in the same spectrum). The absolute Mg II restframe intensity is given at the bottom of Table 4.

For the Fe II emission we list the integrated flux of most of the UV and optical blends and multiplets, using the following designations (e.g., Phillips 1978; Wills et al. 1980) : Fe II 4570: multiplets 37,38,43 (4250 – 4770 \AA), Fe II 4924,5018: multiplet 42 (4800 – 5085 \AA), Fe II 5190: multiplets 42,48,49,55 (5085 – 5500 \AA), Fe II opt total: Fe II flux 4250 – 5500 \AA , Fe II 2080: multiplets UV 83,91,93,94 + Fe III UV 48 (2030 – 2130 \AA), Fe II 2500: multiplets UV 1,3,4,5,35,36,64 (2240 – 2660 \AA), Fe II 2680: multiplets UV 200,235,263,283 (2660 – 2790 \AA), Fe II 2900: multiplets UV 60,78,277,215,231,255 (2790 – 3030 \AA), Fe II UV: total Fe II flux 2200 – 3090 \AA . The multiplets listed are the strongest ones expected in each range. Note that, since the total flux values for entire blends or sums of multiplets often contain additional weak lines, these values are somewhat larger than the sums of the individual prominent blends.

According to Table 4 the mean emission-line ratio of $I(\text{H}\beta\lambda4861) / I(\text{Mg II}\lambda2798)$ for the individual quasars is 1.14 ± 0.16 which, within the uncertainties, is consistent with the relative line strength of $\text{H}\beta$ reported by WNW85 (0.82 ± 0.25). The greater relative strength of $\text{H}\beta\lambda4861$, measured here, might be caused by including a very broad component to measure the line strength. The outer wings of the broad Gaussian component, which we used to determine $I(\text{H}\beta)$, contributes up to $\sim 20\%$ of the total $I(\text{H}\beta)$.

The strength of the Balmer continuum emission (BaC) in units of $I(\text{Mg II}\lambda2798)$ as listed in Table 4 shows some variation between the six high- z quasars. In particular, Q 2227-3928 shows quite weak BaC emission. The relative BaC strength without Q 2227-3928 amounts to $I(\text{BaC})/I(\text{Mg II}) = 5.20 \pm 0.38$. Including Q 2227-3928, the value drops to $I(\text{BaC})/I(\text{Mg II}) = 4.57 \pm 0.71$. However, within the errors the relative BaC emission strength is consistent with the strength we measured for the local mean quasar spectrum, $I(\text{BaC})/I(\text{Mg II})_{\text{local}} = 5.02 \pm 0.51$.

Whether the ratio of the optical-range Fe II-emission of the high- z quasars relative to Mg II differ from the Fe II/Mg II ratio of the local quasar population could not be studied because our local mean quasar spectrum does not cover the optical Fe II emission at $\lambda > 4200 \text{ \AA}$. The average relative strength of the optical Fe II-emission of the six high- z quasars was found to be $I(\text{Fe II opt})/I(\text{Mg II}) = 1.50 \pm 0.16$. This value is in good agreement with the ratio 1.21 ± 0.73 given by WNW85, who studied quasars with $0.12 \leq z \leq 0.63$. This comparison with the WNW 85 Fe II/Mg II ratio for local quasars thus indicates no significant difference, i.e. no evolution of the Fe II/Mg II ratio up to $z \simeq 3.4$.

More interesting is the integral strength of the ultraviolet Fe-emission ($2200\text{--}3090 \text{ \AA}$) relative to Mg II $\lambda2798$. We obtain for the six high- z quasars an average of $I(\text{Fe II UV})/I(\text{Mg II}) = 3.72 \pm 0.20$. Within the uncertainties there is no difference compared with $I(\text{Fe II UV})/I(\text{Mg II}) = 3.82 \pm 0.40$ derived from the local mean quasar spectrum (Tab. 4).

We anticipate that the approach adopted in this work is relatively more accurate than those adopted in the studies by Thompson et al. (1999), Kawara et al. (1996), and Murayama et al. (1999). This is partly due to our use of data with a large, mostly continuous spectral coverage, which allow a much better determination of the underlying continuum. Also, a better account was made of the Balmer continuum emission through a direct fitting thereof; thanks again to the long and continuous spectral coverage. Finally, we use *empirical* UV Fe II emission templates (Boroson & Green 1992; Vestergaard & Wilkes 2001) as opposed to the theoretical templates from the study by WNW85. As discussed by Thompson et al. (1999) the latter approach includes several assumptions on the relative strengths of the emission lines and is clearly an approximation. Although, the relative line strengths, $I(\text{Fe II UV})/I(\text{Mg II})$, measured here are somewhat lower than the Thompson et al., Kawara

et al., and the Murayama et al. quoted values, they are not in immediate contradiction, given the larger uncertainties in the earlier measured values. It is interesting to note that our results are much closer to the $I(\text{Fe II UV})/I(\text{Mg II})$ values predicted by the theoretical models, applied to observed AGN spectra, Netzer & Wills (1983) and WNW85.

By combining the above result for the UV and optical FeII emission we obtain for our high- z quasars $I(\text{Fe II UV} + \text{Fe II opt})/I(\text{Mg II}) = 5.22 \pm 0.29$. This value is lower than most numbers quoted in the literature, but again close to the $I(\text{Fe II}_{tot})/I(\text{Mg II})$ value predicted by theoretical models (Netzer & Wills 1983, WNW85).

The $I(\text{Fe II UV})/I(\text{Mg II})$ ratio which we find for our local quasar sample is comparable to the corresponding value reported for the mean quasar spectrum of the LBQS sample (containing quasars with redshifts in a range of $z \simeq 1 - 2$) with $I(\text{Fe II UV})/I(\text{Mg II}) \simeq 3.7$ (Francis et al. 1991) but below the ratios given by Thompson et al. (1999) (4.3 – 5.3) and Murayama et al. (1999) (8.9). As discussed above, this difference is likely due to our better observational data and the more accurate approach adopted here.

5. Discussion and Conclusion

As pointed out in Section 4 our accurate derivation of the relative Fe II-emission strength for a sample of six high- z quasars, give lower or much lower $I(\text{Fe II UV})/I(\text{Mg II})$ ratios than the values reported in the literature for intermediate and high redshift quasars (e.g., WNW85; Thompson et al. 1999; Murayama et al. 1999). Since the earlier results are consistent with our data to within their higher error limits, we assume that the differences result from our improved multi-component fit of the observed spectra, which was facilitated by the wide wavelength range and accurate calibration of our observational data. On the other hand, the $I(\text{Fe II UV})/I(\text{Mg II})$ ratios for our $z \simeq 3.4$ quasars reported in this paper are comparable to the corresponding mean ratio for low- z quasars, which we determined from the local mean quasar spectrum (Dietrich & Hamann 2001). As our high- z and local quasars do not differ significantly in any other spectral property, it appears unlikely that the strong Fe II emission seen also at $z = 3.4$ can be explained by any other mechanism than comparable relative abundance of Fe in our $z \simeq 3.4$ quasars. Since, as pointed out in Section 1, according to the present chemical evolution theory of galaxies Fe is produced mainly by Type Ia SNe which begin to explode about ~ 1 Gyr after the beginning of star formation, the observed high Fe content of the broad line region (BLR) gas of our quasars confirms that the star formation in the host galaxies of high- z quasars started at a very early epoch.

An evolutionary model of the Fe enrichment in a galaxy following the initial starburst

has been calculated by Yoshii et al. (1998). Although, as pointed out by Yoshii et al., evidence that the initial mass function may have been different for the first stars make such model calculations quantitatively somewhat uncertain, it is clear from these computations that the relative Fe abundance is rather low initially and starts to grow steeply about 1.0 Gyrs after the beginning of the star formation, reaching a maximum (at about 3 Gyrs in the Yoshii et al. model), before declining to the local value (see also Matteucci & Padovani 1993; Hamann & Ferland 1993). The same temporal evolution of the Fe/Mg ratio is found for the giant elliptical galaxy model (M4a) presented by Hamann & Ferland (1993). Their model predicts a strong increase of Fe/H at ~ 1 Gyr after the beginning of the star formation, with the most rapid rise of the Mg/Fe ratio during the 1 - 1.38 Gyrs period. Comparing our relative Fe II emission strength with the model of Yoshii et al. (1998) and Hamann & Ferland (1993) we estimate an age of ~ 1.5 Gyrs (with a formal error of ± 0.5 Gyrs) for the stellar population which produced the observed iron in our high- z quasars. (Because of our smaller Fe II/Mg II emission ratio this value is slightly lower than the corresponding age derived by Yoshii et al. for B 1422+231 at $z = 3.6$). As discussed e.g. by Yoshii et al. (1998) and Thompson et al. (1999) a starburst age of this order and in this redshift range provides severe constraints on the allowed cosmological parameters as realistic cosmologies require a cosmic age at the epoch of the light emission which is larger than the age of the star burst. Like the earlier results of Yoshii et al. (1998) and Thompson et al. (1999) our new data basically rule out cosmologies with $\Omega_M=1$. On the other hand, if the cosmological parameters are known, it is possible to infer from the observed starburst age the redshift at which the star formation started. Although there is still some uncertainty about the cosmological parameters, at present a universe with $H_o = 72 \text{ km s}^{-1} \text{ Mpc}^{-1}$ (Freedman et al. 2001), $\Omega_M=0.3$, $\Omega_\Lambda = 0.7$ appears to be a good approximation. For these parameters the age of the universe at the time when the light was emitted by our $z \simeq 3.4$ quasars was about 1.8 Gyrs. Hence, the star formation age of ~ 1.5 Gyrs derived for our high- z quasars results in an epoch of the beginning of star formation in these objects of ~ 0.3 Gyrs, corresponding (with the above parameters) to $z_f \gtrsim 10$. The redshift z_f can be reduced too if smaller values for H_o and/or Ω_M are assumed. On the other hand, for $\Omega_\Lambda = 0.7$, $\Omega_M = 0.3$ and $H_o > 95 \text{ km s}^{-1} \text{ Mpc}^{-1}$ the age at $z = 3.4$ becomes shorter than the timescale for the production of the observed amount of Fe in SNe type Ia, which seems to rule out such high values of H_o . However, we would like to note that the above age estimates are based on a relatively crude chemical evolution model and on the assumption that the SNe type Ia in the early universe have similar properties as those observed in the local universe. If, as suggested by various theoretical studies, SNe type Ia can, under certain conditions, also be produced by massive stars with a much shorter evolutionary time scale than that assumed in the standard scenarios, some SNe type Ia progenitors could have much shorter life times (e.g., Iben & Tutukov 1984; Smecker-Hane & Wyse 1992). It cannot be excluded that in the

Population III of massive galaxies at early cosmic epochs short-lived SNe type Ia progenitors were more common than in the local universe. In this case the above estimates would provide upper limits only. To constrain the cosmological parameters further it will be important to extend this type of analysis to known QSOs with $z > 5$.

This work has benefited from support of NASA grant NAG 5-3234 and of the Deutsche Forschungsgemeinschaft, project SFB 328 and SFB 439 (MD). MV acknowledges financial support from the Columbus Fellowship.

REFERENCES

- Andreani, P., Franceschini, A., & Granato, G. 1999, MNRAS, 306, 161
- Bautista, M.A. & Pradhan, A.K. 1998, ApJ, 492, 650
- Boroson, T.A. & Green, R.F. 1992, ApJS, 80, 109
- Carilli, C.L., Bertoldi, F., Menten, K.M., et al. 2000, ApJ, 533, L13
- Carlberg, R.G., Yee, H.K.C., Morris, S.L., et al. 1999, ApJ, 516, 552
- Carroll, S.M., Press, W.H., & Turner, E.L. 1992, ARA&A, 30, 499
- Collin, S. & Joly, M. 2000, New Astron.Rev., 44, 531
- Dietrich, M., Appenzeller, I., Wagner, S.J., et al. 1999, A&A, 352, L1
- Dietrich, M. & Wilhelm-Erkens, U. 2000, A&A, 354, 17
- Dietrich, M. & Hamann, F. 2001, in prep.
- Elias, J.H., Frogel, J.A., Matthews, K., & Neugebauer, G. 1982, AJ, 87, 1029
- Elston, R., Thompson, K.L., & Hill, G.J. 1994, Nature, 367, 250
- Francis, P.J., Hewett, P.C., Foltz, C.B., et al. 1991, ApJ, 373, 465
- Freedman, W.L., Madore, B.F., Gibson, B.K., et al. 2001, ApJ, 553, 47
- Ferland, G.J., Baldwin, J.A., Korista, K.T., et al. 1996, ApJ, 461, 683
- Grandi, S.A. 1981, ApJ, 251, 451

- Grandi, S.A. 1982, *ApJ*, 255, 25
- Green, P.J., Forster, K., & Kuraszkiewicz, J. 2001, *ApJ*, 556, 727
- Guilloteau, S., Omont, A., McMahon, R.G., Cox, P., & Petitjean, P. 1997, *A&A*, 328, L1
- Guilloteau, S., Omont, A., McMahon, R.G., Cox, P., & Petitjean, P. 1999, *A&A*, 349, 363
- Hamann, F. & Ferland, G.J. 1992, *ApJ*, 381, L53
- Hamann, F. & Ferland, G.J. 1993, *ApJ*, 418, 11
- Hamann, F. & Ferland, G.J. 1999, *ARA&A*, 37, 487
- Hill, G.J., Thompson K.L., & Elston, R. 1993, *ApJ*, 414, L1
- Horne, K. 1986, *PASP*, 98, 609
- Iben, I., & Tutukov, A.V. 1984, *ApJS*, 54, 335
- Kawara, K., Murayama, T., Taniguchi, Y., & Arimoto, N. 1996, *ApJ*, 470, L85
- Korista, K.T., Hamann, F., Ferguson, J., & Ferland, G.J. 1996, *ApJ*, 461, 641
- Kuhn, O., Elvis, M., Bechtold, J., & Elston, R. 2001, *ApJ*, in press
- Kurucz, R.L. 1992, in *The Stellar Populations of Galaxies*, IAU Symp. # 149, eds. B. Barbury, A. Renzini, Kluwer Dordrecht, p.225
- Laor, A., Jannuzi, B.T., Green, R.F., & Boroson, T.A. 1997, *ApJ*, 489, 656
- Malkan M.A. & Sargent W.L.W. 1982, *ApJ*, 254, 22
- Matteucci, F. & Greggio, L. 1986, *A&A*, 154, 279
- Matteucci, F. & Padovani, P. 1993, *ApJ*, 419, 485
- McIntosh, D.H., Rieke, M.J., Rix, H.-W., Foltz, C.B., & Weymann, R.J. 1999, *ApJ*, 514, 40
- Murayama, T., Taniguchi, Y., Evans, A.S., et al. 1998, *AJ*, 115, 2237
- Murayama, T., Taniguchi, Y., Evans, A.S., et al. 1999, *AJ*, 117, 1645
- Netzer, H. & Wills, B.J. 1983, *ApJ*, 275, 445
- Netzer, H., Wamsteker, W., Wills, B.J., & Wills, D. 1985, *ApJ*, 292, 143

- Netzer H. & Laor A. 1993, ApJ, 404, L51
- Omont, A., Cox, P., Bertoldi, F., McMahon, R.G., Carilli, C.L., & Isaak, K.G. 2001, A&A, 374, 371
- Osmer, P.S. & Shields, J.C. 1999, in ‘Quasars and Cosmology’, ASP Conf.Ser.162, eds. G.Ferland & J.A.Baldwin, p.235
- Perlmutter, S., Aldering, G., Goldhaber, G., et al. 1999, ApJ, 517, 565
- Perryman, M.A.C., Lindegren, L., Kovalevsky, J., et al. 1997, A&A, 323, L49
- Peterson B.M. 1997, in ‘An Introduction to Active Galactic Nuclei’, Cambridge University Press, p.156
- Pettini, M. 1999, in Proc.of ESO Workshop ‘Chemical Evolution from Zero to High Redshift’, ed. J. Walsh & M. Rosa, LNP, p.233
- Phillips M.M. 1978, ApJS, 38, 187
- Sanders, D.B., Phinney, E.S., Neugebauer, G., Soifer, B.T., & Matthews, K. 1989, ApJ, 347, 29
- Smecker-Hane, T.A., & Wyse, R.F.G. 1992, AJ, 103, 1621
- Sigut, T.A.A. & Pradhan, A.K. 1998, ApJ, 499 L139
- Storey, P.J. & Hummer, D.G. 1995, MNRAS, 272, 41
- Taniguchi, Y., Murayama, T., Kawara, K., & Arimoto, N. 1997, PASJ, 49, 419
- Thompson, K.L., Hill, G.J., & Elston, R. 1999, ApJ, 515, 487
- Tinsley, B.M. 1979, ApJ, 229, 1046
- Verner, E.M., Verner D.A., Korista, K.T., et al. 1999, ApJS, 120, 101
- Véron-Cetty, M.-P. & Véron, P. 2001, A Catalogue of Quasars and Active Nuclei, 10th edition
- Vestergaard, M. & Wilkes, B.J. 2001, ApJS, 134, 1
- Wampler, E.J. & Oke, J.B. 1967, ApJ, 148, 695
- Wheeler, J.C., Sneden, C., & Truran, J.W. 1989, ARA&A, 27, 279

- Willott, C.J., Rawlings, S., Jarvis, M.J. 2000, MNRAS, 313, 237
- Wills, B.J., Netzer, H., Uomoto, A.K., & Wills, D. 1980, ApJ, 237, 319
- Wills, B.J., Netzer, H., & Wills, D. 1985, ApJ, 288, 94
- Yoshii, Y., Tsujimoto, T., & Nomoto, K. 1996, ApJ, 462, 266
- Yoshii, Y., Tsujimoto, T., & Kawara, K. 1998, ApJ, 507, L113

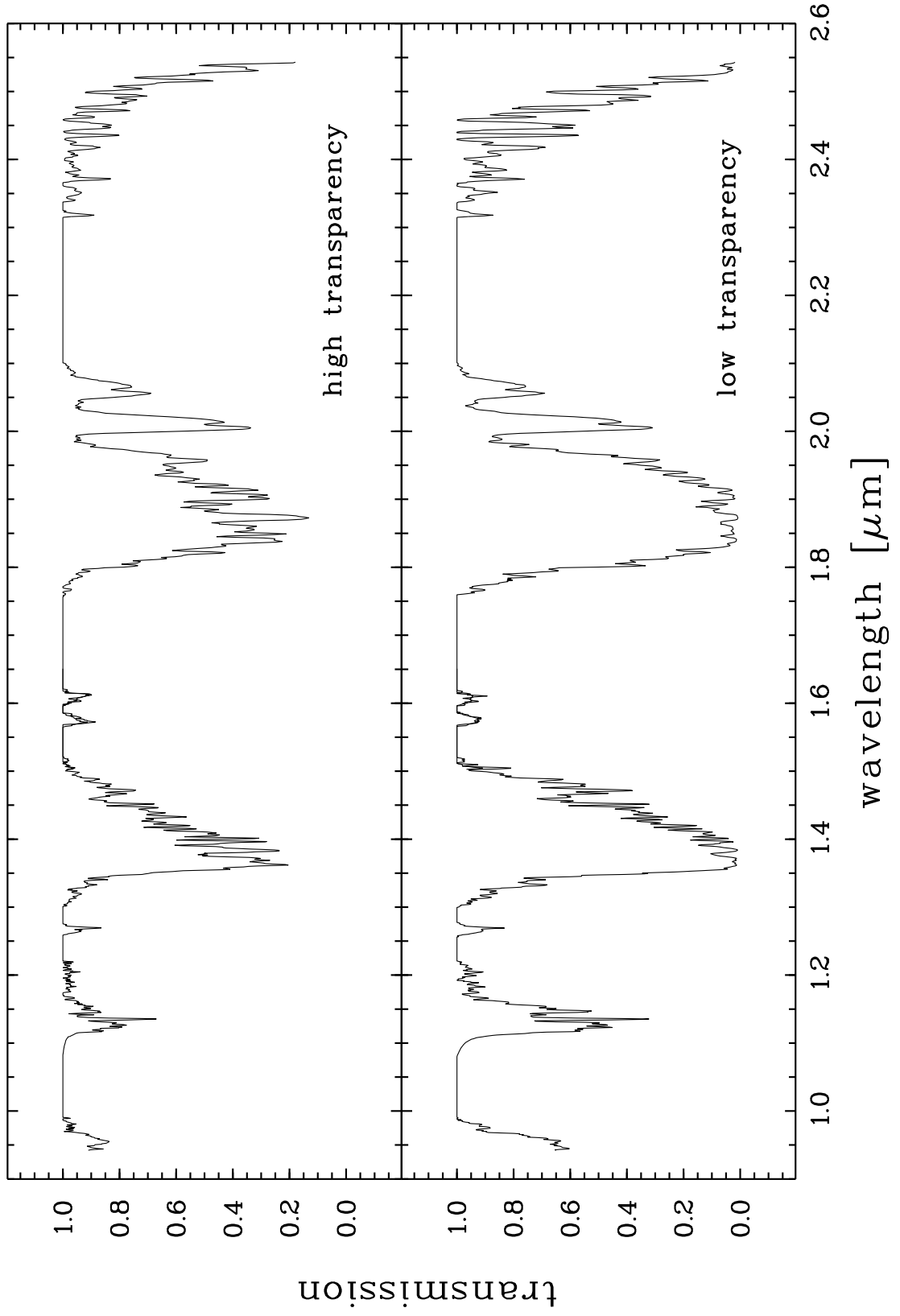
Fig. 1.— The atmospheric transmission during the observing run obtained from the standard stars as a function of wavelength for optimal conditions (top panel) and poor conditions (bottom panel).

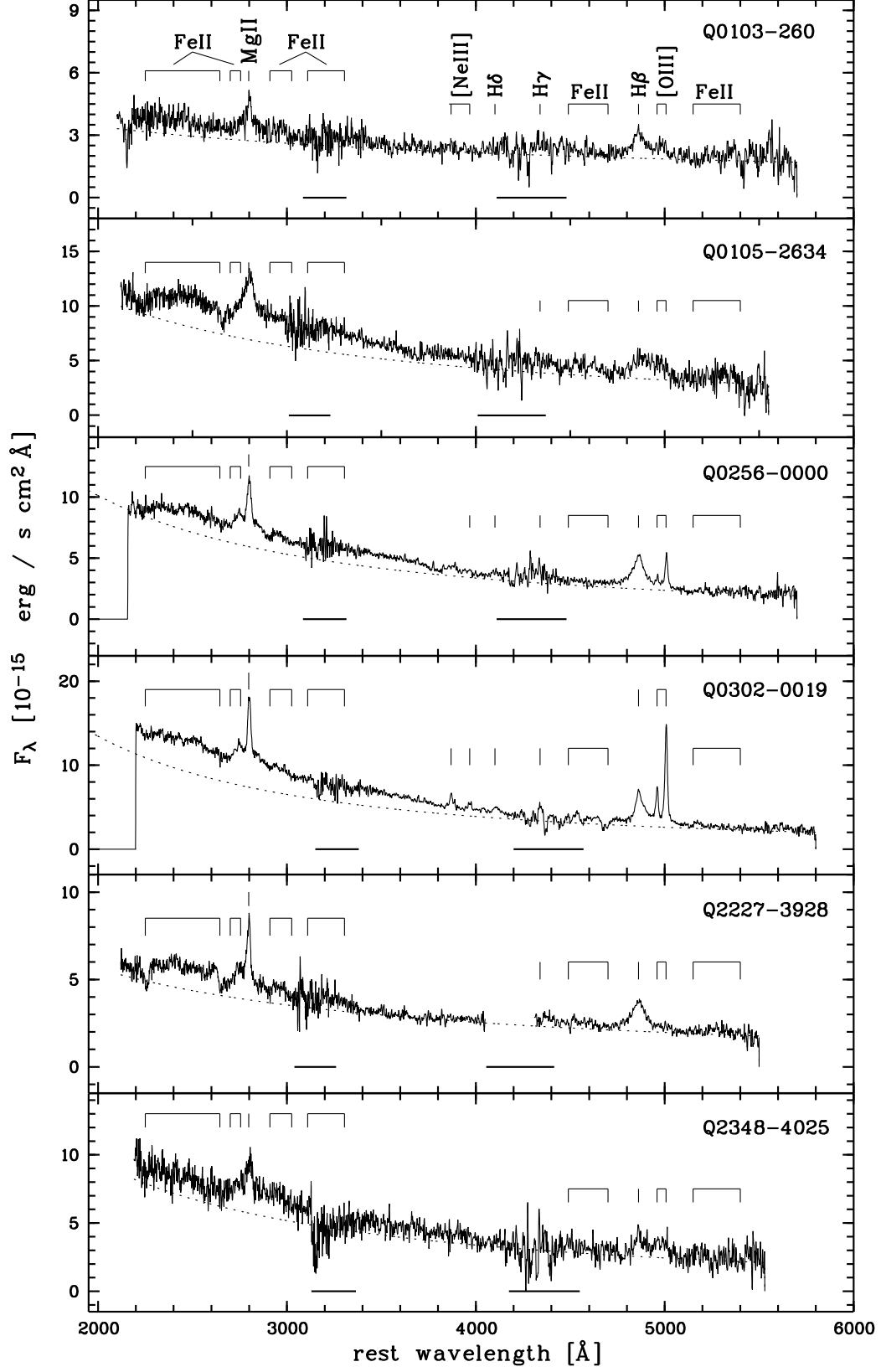
Fig. 2.— The quasar spectra transformed to the restframe. The flux density is given in units of $10^{-15} \text{ erg s}^{-1} \text{ cm}^{-2} \text{ \AA}^{-1}$. The location of the strong atmospheric absorption bands is indicated by the horizontal bars for each quasar.

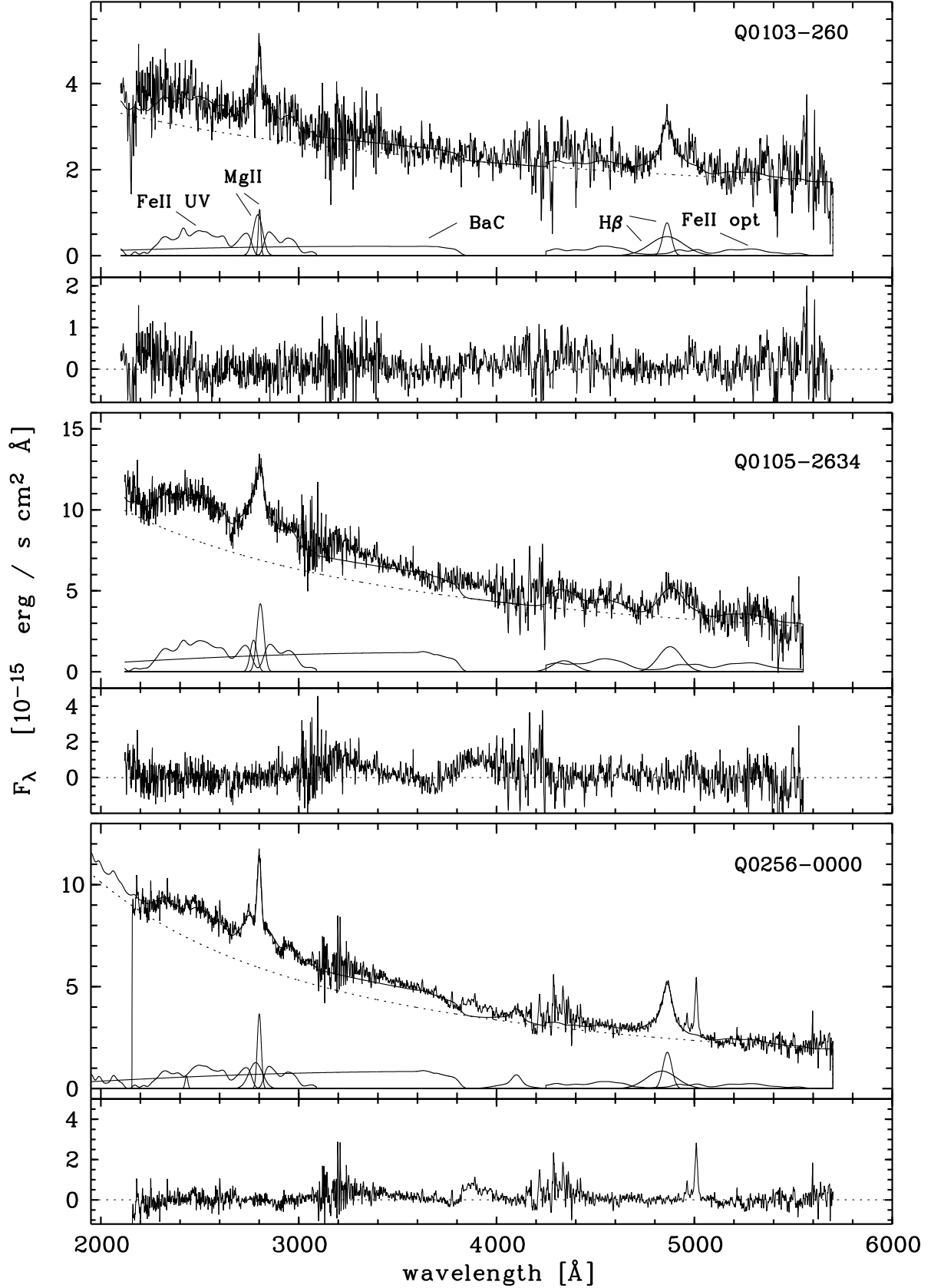
Fig. 3.— The restframe quasar spectra together with results of the multi-component analysis are shown for Q 0103-260, Q 0105-2634, and Q 0256-0000. In the top panel the quasar spectrum is shown together with the power law continuum fit (dotted line), the scaled and broadened Fe-emission template, the scaled Balmer continuum emission, and the Gaussian components to fit the $\text{Mg II } \lambda 2798$ and $\text{H } \beta \lambda 4861$ emission line profiles. The resulting fit is overplotted as a solid line. In the bottom panel the quasar spectrum is shown after subtraction of these components.

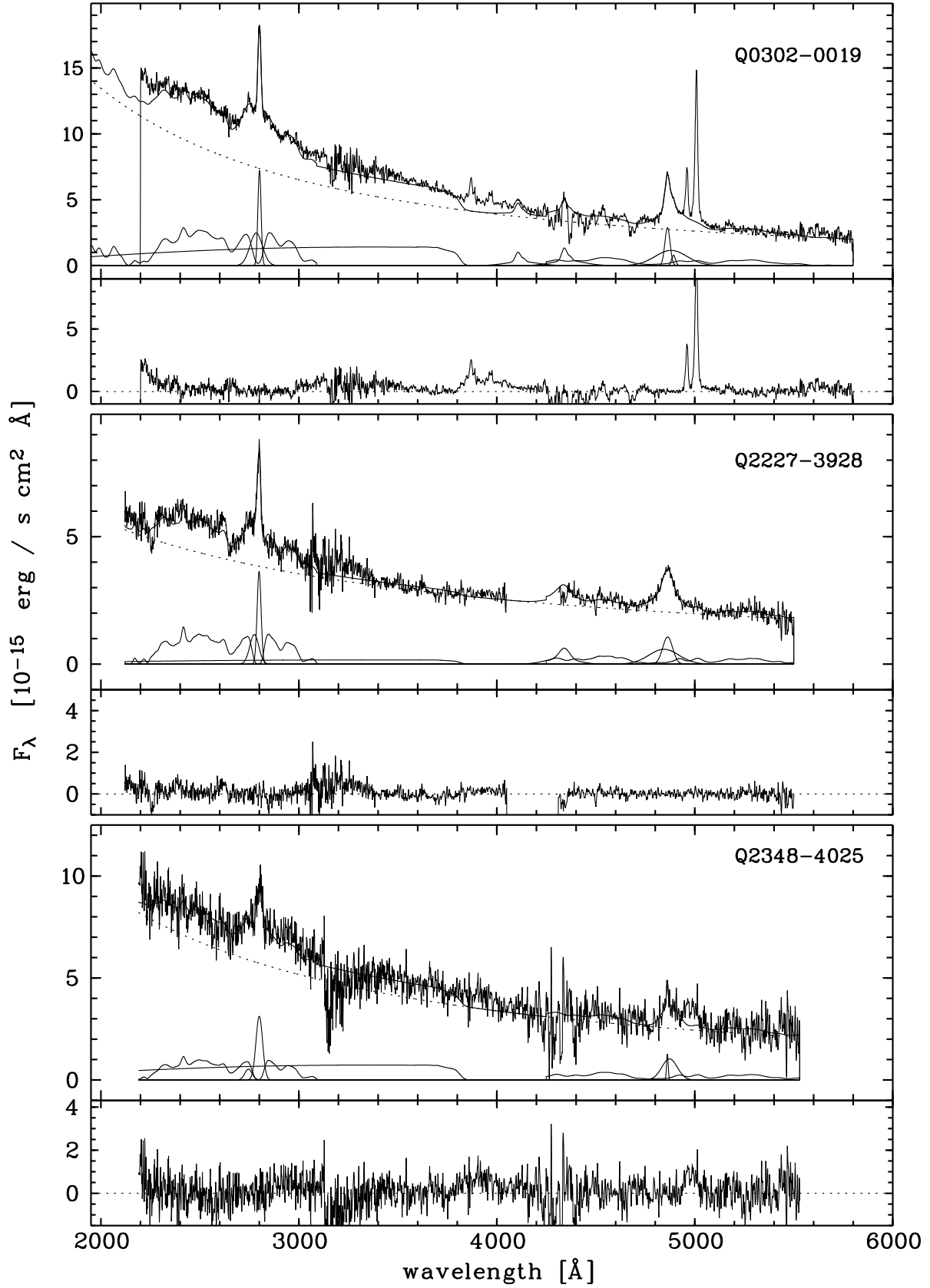
Fig. 4.— Same as Fig. 3 for Q 0302-0019, Q 2227-3928, and Q 2348-4025.

Fig. 5.— Same as Fig. 3 for the local mean quasar spectrum.









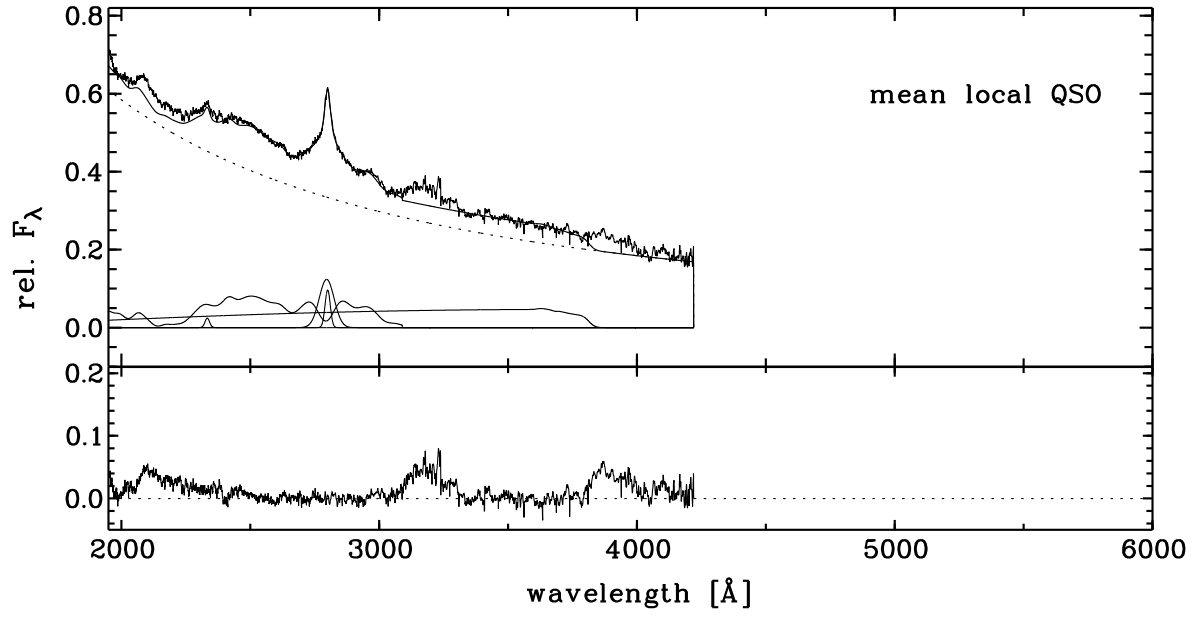


Table 1. The quasars sample

object (1)	RA(J2000.0) (2)	DEC(J2000.0) (3)	app.mag. ^a (4)	z (5)
quasar	<i>h m s</i>	<i>° ′ ″</i>	m_r	
Q 0103-260	01 06 04.3	−25 46 53	18.82	3.375
Q 0105-2634	01 08 12.4	−26 18 20	17.30	3.488
Q 0256-0000	02 59 05.6	+00 11 22	17.50	3.377
Q 0302-0019	03 04 49.9	−00 08 13	17.60	3.286
Q 2227-3928	22 30 32.9	−39 13 07	18.60	3.438
Q 2348-4025	23 51 16.1	−40 08 36	18.10	3.310
star			m_K ^b	type
HD 19904	03 10 43	−39 03 06	6.64	A4III/IV
HD 25402	04 00 32	−41 44 54	8.36 ^c	G3V
HD 38921	05 47 22	−38 13 52	7.54	A0V
HD 205772	21 38 41	−41 02 53	7.66	A5IV/V
HD 210395	22 11 02	−39 32 51	7.98 ^c	G3V

^aVéron-Cetty & Véron (2001)

^bElias et al. (1982)

^c m_v

Table 2. observation log

object	$\lambda\lambda$ -range	date	t_{int} [sec]	no.of exp.	total $_{int}$ [sec]	comment
(1)	(2)	(3)	(4)	(5)	(6)	(7)
Q 0103-260	blue	Oct. 19/20	240	12	2880	seeing $\sim 0''.8$
	red	Oct. 19/20	240	18	4320	seeing $\sim 0''.6$
	blue	Oct. 20/21	240	8	1920	
	red	Oct. 20/21	240	10	2400	
Q 0105-2634	blue	Oct. 20/21	240	12	2880	seeing $\sim 1''.1$
	red	Oct. 20/21	240	6	1440	seeing $\sim 1''.2$
Q 0256-0000	blue	Oct. 19/20	240	12	2880	seeing $\sim 0''.7$
	red	Oct. 20/21	240	12	2880	seeing $\sim 1''.2$
	blue	Oct. 21/22	180	14	2520	seeing $\sim 2''.2$, clouds
	red	Oct. 21/22	180	3	540	clouds
Q 0302-0019	blue	Oct. 19/20	240	12	2880	seeing $\sim 0''.6$
	red	Oct. 19/20	240	15	3600	seeing $\sim 0''.7$
	blue	Oct. 20/21	240	12	2880	seeing $\sim 1''.0$
	red	Oct. 20/21	240	12	2880	seeing $\sim 1''.0$
Q 2227-3928	blue	Oct. 19/20	180	16	2880	seeing $\sim 1''$
	red	Oct. 19/20	180	8	1440	
	blue	Oct. 20/21	240	6	1440	
	red	Oct. 20/21	240	10	2400	
	blue	Oct. 21/22	240	5	1200	seeing $\sim 1''.4$, clouds
	red	Oct. 21/22	240	12	2880	seeing $\sim 1''.6$
	blue	Oct. 20/21	240	6	1440	seeing $\sim 2''.0$
	red	Oct. 20/21	240	6	1440	seeing $\sim 1''.5$
Q 2348-4025	blue	Oct. 21/22	240	6	1440	seeing $\sim 1''.7$, clouds
	red	Oct. 21/22	240	12	2880	seeing $\sim 1''.7$, clouds
	blue	Oct. 22/23	180	16	2880	clouds
	red	Oct. 22/23	180	16	2880	clouds
HD 19904	blue	Oct. 19/20	5	4	20	seeing $\sim 0''.5$
	red	Oct. 19/20	5	4	20	
	blue	Oct. 20/21	5	4	20	seeing $\sim 1''.5$
	red	Oct. 20/21	5	4	20	

Table 2—Continued

object	$\lambda\lambda$ -range	date	t_{int} [sec]	no.of exp.	$total_{int}$ [sec]	comment
(1)	(2)	(3)	(4)	(5)	(6)	(7)
HD 25402	blue	Oct. 19/20	5	4	20	
	red	Oct. 19/20	5	4	20	seeing $\sim 0''.6$
	blue	Oct. 20/21	5	4	20	seeing $\sim 1''.2$
	red	Oct. 20/21	5	4	20	
HD 38921	blue	Oct. 19/20	5	4	20	seeing $\sim 0''.6$
	red	Oct. 19/20	5	4	20	
HD 205772	blue	Oct. 19/20	10	8	80	
	blue	Oct. 19/20	5	4	20	
	red	Oct. 19/20	5	4	20	
	blue	Oct. 20/21	5	4	20	
	red	Oct. 20/21	5	4	20	
	blue	Oct. 21/22	5	4	20	clouds
	red	Oct. 21/22	5	4	20	clouds
	blue	Oct. 22/23	5	8	40	
	blue	Oct. 19/20	5	4	20	
	red	Oct. 19/20	5	4	20	
HD 210395	blue	Oct. 20/21	5	4	20	
	red	Oct. 20/21	5	4	20	
	blue	Oct. 21/22	5	8	40	clouds
	red	Oct. 21/22	5	8	40	clouds

Table 3. total and effective integration times

quasar (1)	t_{tot}^{blue} (2)	t_{eff}^{blue} (3)	t_{tot}^{red} (4)	t_{eff}^{red} (5)
Q 0103-260	4800	4800	6720	4560
Q 0105-2634	2880	2880	1440	1440
Q 0256-0000	5400	2880	3420	2880
Q 0302-0019	5760	5760	6480	6000
Q 2227-3928	5520	4320	6720	5760
Q 2348-4025	5760	3720	4320	2160

Table 4. emission line measurements

feature	Q 0103-260	Q 0105-2634	Q 0256-0000	Q 0302-0019	Q 2227-3928	Q 2348-4025	local QSO
C II]2326	—	—	—	—	—	—	0.05±0.01
[Ne IV]2423	—	—	0.05±0.01	—	—	—	—
Mg II2798	1.00±0.05	1.00±0.04	1.00±0.03	1.00±0.03	1.00±0.03	1.00±0.06	1.00±0.05
[Ne III]3869	—	—	—	0.13±0.02	—	—	—
H δ 4101	—	—	0.34±0.04	0.26±0.04	—	—	—
H γ 4340	0.52±0.11	0.37±0.06	—	0.34±0.05	0.43±0.08	—	—
H β 4861	1.84±0.13	0.84±0.07	1.32±0.08	1.01±0.05	1.12±0.07	0.73±0.08	—
[O III]4959	0.03:	—	0.06±0.01	0.18±0.01	—	—	—
[O III]5007	0.10:	—	0.22±0.02	0.59±0.02	0.015:	—	—
Fe II4570 ^a	0.99±0.16	1.01±0.13	0.57±0.06	0.58±0.07	0.64±0.09	0.78±0.10	—
Fe II4924,5018 ^b	0.36±0.06	0.37±0.05	0.21±0.02	0.22±0.03	0.24±0.03	0.28±0.04	—
Fe II5190 ^c	0.58±0.09	0.59±0.08	0.33±0.03	0.34±0.04	0.38±0.05	0.46±0.06	—
Fe II opt ^d	1.95±0.31	1.99±0.26	1.12±0.11	1.15±0.14	1.26±0.17	1.53±0.19	—
Fe II2080 ^e	—	—	0.18±0.02	—	—	—	0.23±0.02
Fe II2500 ^f	2.43±0.29	2.26±0.26	1.73±0.15	2.44±0.23	2.29±0.24	1.94±0.23	2.25±0.23
Fe II2680 ^g	0.59±0.07	0.54±0.06	0.42±0.04	0.59±0.06	0.55±0.06	0.47±0.06	0.54±0.06
Fe II2900 ^h	1.03±0.12	0.95±0.11	0.73±0.06	1.03±0.10	0.96±0.10	0.82±0.10	0.95±0.10
Fe IIUV ⁱ	4.14±0.50	3.84±0.44	2.95±0.26	4.16±0.40	3.90±0.40	3.31±0.38	3.82±0.40
Fe IIUV/Fe II opt	2.13±0.40	1.93±0.33	2.64±0.33	3.62±0.53	3.10±0.51	2.16±0.32	—
Fe IIUV + Fe II opt	6.09±0.68	5.83±0.63	4.07±0.36	5.31±0.50	5.15±0.53	4.84±0.55	—
Balmer cont. ^j	3.86±0.60	5.45±0.60	5.15±0.50	5.40±0.49	1.37±0.14	6.16±0.67	5.02±0.51
τ_{BaC}	1.0	0.5	0.5	1.0	1.0	1.0	1.0
α	-1.33±0.06	-0.69±0.06	-0.41±0.05	-0.21±0.03	-0.85±0.05	-0.53±0.07	-0.34±0.03

Table 4—Continued

feature	Q 0103-260	Q 0105-2634	Q 0256-0000	Q 0302-0019	Q 2227-3928	Q 2348-4025	local QSO
$I_{rest}(\text{Mg II } \lambda 2798)$ [$10^{-15} \text{erg s}^{-1} \text{cm}^{-2}$]	73.6 ± 3.5	267.4 ± 11.0	200.7 ± 7.0	341.5 ± 10.0	156.0 ± 5.0	155.6 ± 10.0	317.2 ± 16.7

^a $\lambda\lambda 4250 - 4770 \text{ \AA}$, ^b $\lambda\lambda 4800 - 5085 \text{ \AA}$, ^c $\lambda\lambda 5085 - 5500 \text{ \AA}$, ^d $\lambda\lambda 4250 - 5500 \text{ \AA}$, ^e $\lambda\lambda 2030 - 2130 \text{ \AA}$, ^f $\lambda\lambda 2240 - 2660 \text{ \AA}$,
^g $\lambda\lambda 2660 - 2790 \text{ \AA}$, ^h $\lambda\lambda 2790 - 3030 \text{ \AA}$, ⁱ $\lambda\lambda 2200 - 3090 \text{ \AA}$, ^j $\lambda\lambda 2200 - 3650 \text{ \AA}$